

Real-Time mmWave Channel Sounding Through Switched Beamforming With 3-D Dual-Polarized Phased-Array Antennas

Derek Caudill¹, Jack Chuang¹, Sung Yun Jun¹, *Member, IEEE*, Camillo Gentile¹, *Member, IEEE*, and Nada Golmie, *Senior Member, IEEE*

Abstract—We propose a 28.5-GHz channel sounder that switches through all antennas of multiple dual-polarized 8×8 phased arrays at the transmitter and receiver and performs beamforming in postprocessing through digital weights to synthesize a sweepable beam. To our knowledge, we are the first to implement—what we refer to as—*switched beamforming* with phased arrays for millimeter-wave channel sounding, realized through highly stable Rubidium clocks and local oscillators coupled with precision over-the-air calibration techniques developed in house. By circumventing the time-consuming programming of analog weights that is associated with analog beamforming—what phased arrays are designed for—we can sweep a 3-D double-omnidirectional dual-polarized channel in just 1.3 ms, for real-time sounding. By in turn circumventing the coarse precision of analog weights, we can synthesize ideal beam patterns thanks to the effectively infinite precision of digital weights, enabling fine weight calibration for the nonidealities of the system hardware and fine weight tapering for sidelobe suppression. This translates to average estimation errors of 0.47° in 3-D double-directional angle, 0.48 dB in co-polarized path gain, and 0.18 ns in delay, as substantiated by field measurements.

Index Terms—Calibration, channel sounder, 5G, millimeter wave (mmWave), propagation, 285 GHz.

I. INTRODUCTION

THE wireless propagation channel can be modeled as a discrete set of paths (also known as rays or multipath components) representing plane waves¹ propagating from the transmitter (T) to the receiver (R) [1]. The ultimate objective in channel sounding is to exhaustively characterize the properties of each path n [2], namely its:

- 1) 3-D double-omnidirectional angle (θ_n^T, θ_n^R) , where $\theta_n^T = (\theta_n^{T,A}, \theta_n^{T,E})$ is the angle of departure (AoD) from T in azimuth (A) and elevation (E) and $\theta_n^R = (\theta_n^{R,A}, \theta_n^{R,E})$ is the angle of arrival (AoA) to R, with omnidirectional field of view (FoV) at both ends;

- 2) polarization-dependent path gain PG^{pq} , where p and q is either vertical (V) or horizontal (H) polarization at T and R respectively;

- 3) delay τ_n .

Since the millimeter-wave (mmWave) channel suffers from much greater path loss than its microwave counterpart, 5G systems will employ high gain—and by corollary narrowbeam—antennas to compensate the link budget. The first mmWave channel sounders employed horn antennas [3]–[10] that were swept in azimuth and elevation through mechanical rotation at both ends. To obtain polarization-dependent path gain, either two (V and H) polarized horns were deployed at each end [11] or a single horn was additionally rotated 90° in pitch [12]. An alternative implementation to mechanical rotation is mechanical translation on a positioner [13] or robotic arm [14] to form a virtual (or synthetic) phased-array antenna whose beam is swept in postprocessing, *i.e.*, by applying digital complex weights to the antenna responses to synthesize a virtual beam.

What constrains these systems is the slow mechanical movement, necessitating minutes to hours to even days for a single channel sweep, limiting measurement campaigns typically to tens of acquisitions. A more pressing implication of mechanical movement is that only static environments can be sounded—precluding mobile and outdoor scenarios—since the channel must be swept within the channel coherence time, the time over which the channel is considered stationary. mmWave communications systems are expected to operate at channel bandwidths up to 2 GHz or even wider with channel bonding [15]. The maximum coherence distance at 2 GHz is 7.5 cm [16], which at a nominal vehicular speed of 50 km/h translates to a coherence time of 5 ms.

The emergence of mmWave phased-array antennas [17]–[21] in recent years has prompted migration from horn antennas for channel sounding. Phased arrays are designed for analog beamforming (ABF), *i.e.*, applying complex weights to the array antennas by programming the amplifiers and phased shifters on the printed circuit boards to synthesize an electronic beam. Besides featuring high narrowbeam gain, the beam can be swept electronically rather than mechanically to enable much faster channel sweep durations. An additional advantage is their flexibility in shaping the beam pattern (beamwidth, sidelobe suppression through

Manuscript received March 12, 2021; revised May 17, 2021; accepted July 15, 2021. (Corresponding author: Camillo Gentile.)

Derek Caudill and Sung Yun Jun are with the RF Technology Division, National Institute of Standards and Technology, Boulder, CO 80305 USA.

Jack Chuang, Camillo Gentile, and Nada Golmie are with the Wireless Networks Division, National Institute of Standards and Technology, Gaithersburg, MA 20899 USA (e-mail: camillo.gentile@nist.gov).

Color versions of one or more figures in this article are available at <https://doi.org/10.1109/TMTT.2021.3104278>.

Digital Object Identifier 10.1109/TMTT.2021.3104278

¹Under the far-field assumption, T and R are at least 10–20 wavelengths apart from each other and from any ambient scatterers.

TABLE I
MMWAVE PHASED-ARRAY ANTENNA CHANNEL SOUNDERS TO DATE

Affiliation	Center frequency (GHz)	Channel sweep duration	Channel sweep type	Sweep angle (deg.)	Azimuth FoV (deg.)	Elevation FoV (deg.)	Polarizations
USC [24][26]	28	1.4 ms	2-D double	5	90	60	VV
AT&T [27]	28	6.25 ms	3-D single	16.8	360	60	VV
NCSU [28]	28	3.4 s	3-D double	20	90	40	VV
NIST [29][30]	60	262 μ s	2-D double	5.6	360	11.6	VV
NYU [31][32]	60	1 ms	2-D double	7.5	90	20	VV
Fraunhofer [33]	60	10 s	3-D single	5	90	30	VV
GhentU [34] / NEU [35]	60	5 min	2-D double	2.8	90	12.0	VV

tapering, placing nulls, and so on). Finally, their miniature form factor permits both V- and H-polarized antennas on the same board [22]–[24]. Table I lists the phased-array-based mmWave channel sounders in the literature to date [24]–[35]. They exhibit a wide range of channel sweep duration, from microseconds to minutes depending on the sweep type (2-D or 3-D and single or double directional), sweep angle, FoV, and polarizations.

Yet, none of the systems can complete a 3-D double-omnidirectional sweep within milliseconds, nor implement dual polarization. This is due to ABF, which has two important limitations:

- 1) *ABF Channel Sweep Duration*: Programming the complex weights across all array antennas typically takes at least 1 ms per beam but can take up to hundreds of milliseconds. In turn, sweeping the beam in azimuth and elevation across the FoV of each array per polarization can easily multiply 1 ms to seconds or minutes, depending on the channel sweep type and sweep angle, as evidenced in Table I.
- 2) *ABF Beam Quality*: The gain and phase state of each complex weight has coarse precision, usually between 4 and 8 bits, so the beam shape is limited by design *a priori* and moreover in its ability to compensate for hardware nonidealities through weight calibration, lending to beams that are asymmetrical and have poor sidelobe suppression, double lobes, and so on. This in turn degrades the angle estimation of the paths.

In this article, we propose a 28.5-GHz channel sounder that, instead of sweeping beams through ABF, switches through the antennas of multiple dual-polarized 8×8 phased arrays at the transmitter and receiver and performs—what we refer to as—*switched beamforming* (SBF) in postprocessing. To our knowledge, we are the first to implement SBF with phased arrays, enabled through highly stable Rubidium clocks and local oscillators (LOs) coupled with precision over-the-air (OTA) calibration techniques developed in house. The two main contributions of our work, each overcoming an ABF limitation listed above, are given in the following:

- 1) *SBF Channel Sweep Duration*: By circumventing the weight programming inherent to ABF, we can sweep a 3-D double-omnidirectional dual-polarized channel in just 1.3 ms, to realize mobile channel sounding.
- 2) *SBF Beam Quality*: Through the effectively infinite precision of digital weights, we can obtain ideal beam patterns through fine weight calibration for the nonidealities of the system hardware and through fine tapering for sidelobe suppression, translating to an average angle estimation error of 0.47° , as substantiated by field measurements.

The remainder of this article is developed as follows: Section II describes the system architecture and Section III describes the techniques developed to calibrate the system. Section IV describes the algorithm we implement to extract the channel paths and their properties from the measurements, followed by illustrative results in Section V and conclusions in Section VI.

II. SYSTEM ARCHITECTURE

The architecture of the channel sounder and its operation are described in this section. First, we describe the phased-array antennas, which form the heart of the system, followed by the transmitter and receiver sections. Then, we describe how the channel is swept, and finally, how the channel measurements are collected autonomously by a mobile robot at the receiver.

A. Phased-Array Antennas

Fig. 1(a) shows the dual-polarized 8×8 phased-array antenna boards integrated in our channel sounder. Here, we just highlight their main characteristics, while specific details can be found in [23], [24]. Each of the 64 elements features stacked V- and H-polarized microstrip antennas (MSAs). The arrays have separate RF ports per polarization, providing cross-polarization rejection of at least 35 dB. The null-to-null bandwidth is 4 GHz and is centered at 28.5 GHz, corresponding to $\lambda = 10.5$ mm. The antennas are spaced roughly at $\lambda/2$ —5.1 mm in azimuth and 6.3 mm in elevation—and the magnitude and phase of each of the

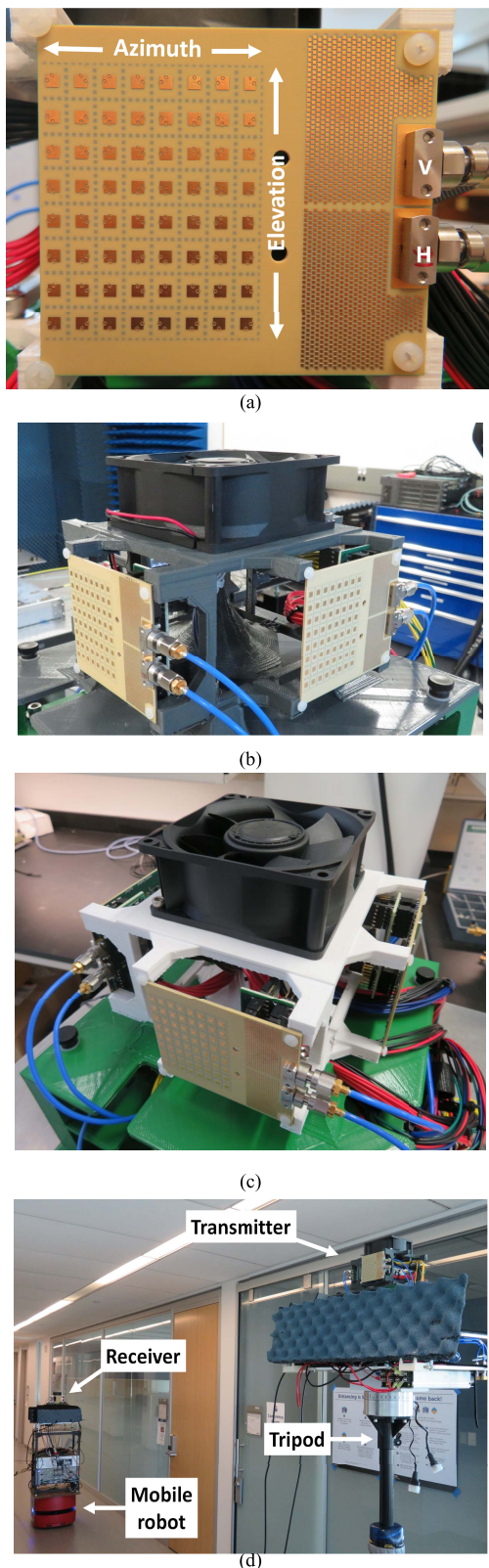


Fig. 1. Photograph of channel sounder. (a) Dual-polarized 8×8 phased-array antenna board. Each element has stacked V- and H-polarized MSAs. The two polarizations have separate feeds. (b) Transmitter section. (c) Receiver section. (d) Transmitter section mounted on tripod and receiver section mounted on a mobile robot.

128 (64×2) antennas can be independently programmed through a serial peripheral interface (SPI), with 8-bit magnitude precision and 6-bit phase precision. The SPI also features

a channel select register to toggle each antenna ON/OFF via its DC amplifier, to allow for separate antenna calibration. (The SPI port is on the back of the array.) The arrays can sweep beams $\pm 45^\circ$ in azimuth and $\pm 25^\circ$ in elevation.

B. Transmitter (T) Section

Since each array can only sweep $\pm 45^\circ$ in azimuth, two arrays were arranged at a right angle on the T section, as shown in Fig. 1(b), to render a combined 180° azimuth FoV. During field operation, the T section is mounted on a tripod with its “blind side” oriented away from the R section, so the limited azimuth FoV is acceptable. The central fan (black box) is critical for heat dissipation. Absorber was attached to the metal plates below the arrays to minimize reflection from the system into the measured channel.

A block diagram of the T section is shown in Fig. 2(a). Each of the two arrays is driven by separate arbitrary waveform generators (AWGs) that have two channels each to accommodate both polarizations. The AWG generates a repeating BPSK-modulated m -ary pseudorandom-noise (PN) code per channel, with 0.5-ns chip length (2-GHz half-power bandwidth) and 2047 chips (33-dB processing gain). The code is synthesized at an intermediate frequency (IF) of 4 GHz and mixed with an LO digitally tuned to 12.25 GHz, followed by a frequency doubler for upconversion to precisely 28.5 GHz. Finally, the RF signal is fed via a power amplifier (PA) to an RF port of an array at approximately 8.8-dBm transmit power.

C. Receiver (R) Section

In contrast to the fixed T section, omnidirectional azimuth FoV is critical at R since it is mounted on a mobile robot and so must be able to “see” from any robot heading when in motion. To that end, four arrays were arranged at right angles. Fig. 1(c) shows a photograph of the R section and Fig. 2(b) shows its block diagram. For every code transmitted, all four arrays receive on both polarizations simultaneously, accommodated by an oscilloscope with eight channels. The received RF signal per port is fed to a low noise amplifier (LNA), downconverted back to IF via the LO, and sampled directly at 16 GHz, as opposed to on-the-fly correlation that some channel sounders implement [5]. The advantage of the former is that correlation with the known PN code is performed in postprocessing so that the channel can be sampled quicker. The correlation yields the complex channel impulse response (CIR) $y(\tau)$. Three codes are averaged to boost the processing gain from 33 to 37.8 dB. Rubidium clocks at T and R were employed for synchronous transmission and sampling between the two ends, and to discipline the LOs.

D. Channel Sweep

Phased-array antennas—including ours—are designed to synthesize an electronic beam by coherently phasing the antennas through ABF, by programming their analog weights through the SPI controller. The beam is swept electronically by programming the weights each time. The drawback of beam sweeping is that programming is time-consuming; for

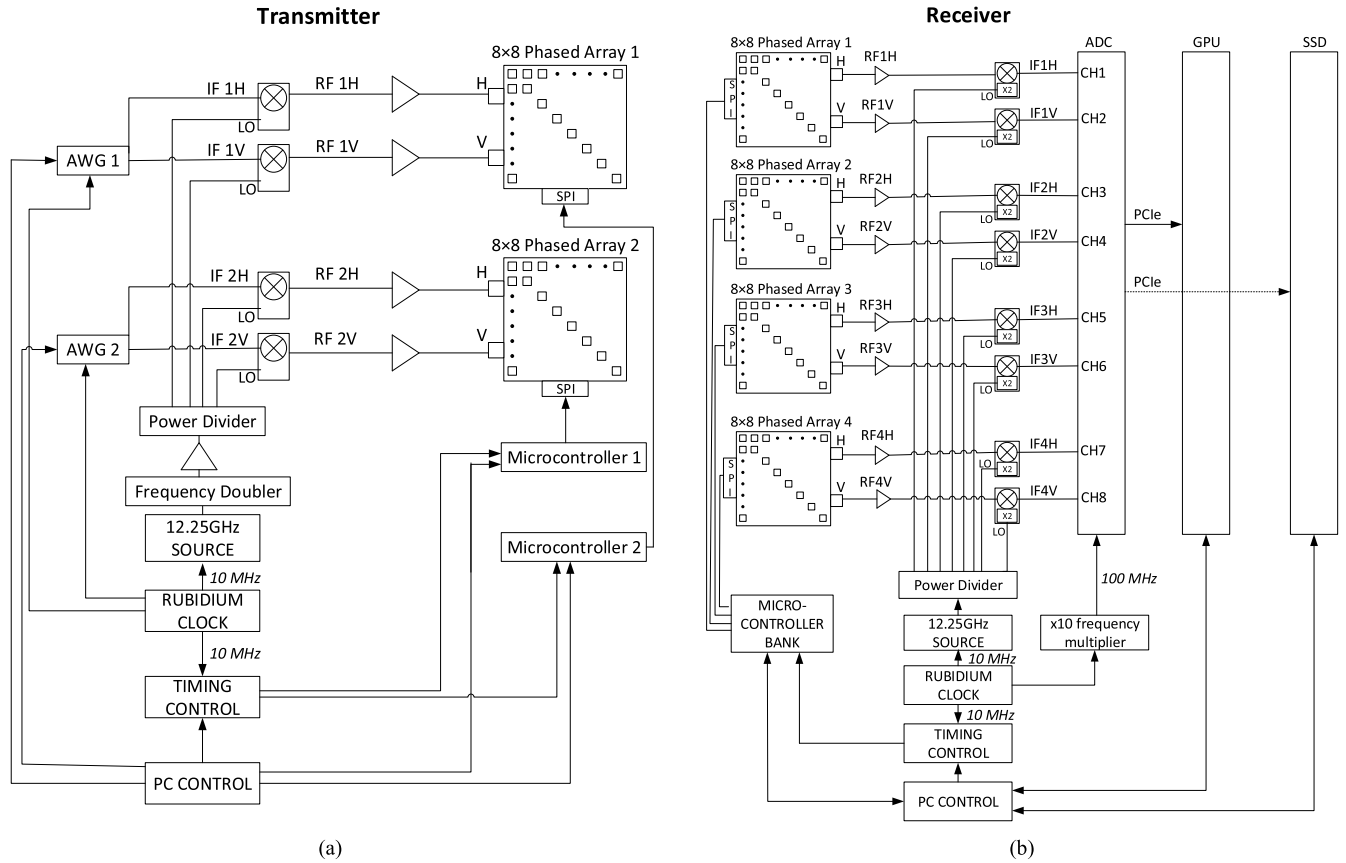


Fig. 2. Block diagrams of (a) transmitter (T) section and (b) receiver (R) section.

our arrays, it takes $3.5 \mu\text{s}$ to program each antenna or, equivalently, $3.5 \mu\text{s} \times 64 = 224 \mu\text{s}$ to program a beam across all 64 antennas per array per polarization. To obtain the best angular estimation possible, it is desirable to sweep the beam at the finest angle possible, which for our arrays is 1.8° in azimuth and 1.4° in elevation given the 6-bit phase precision. This translates to sweeping $50 \times 36 = 1800$ beams within the $\pm 45^\circ$ azimuth and $\pm 25^\circ$ elevation FoV, requiring $224 \mu\text{s} \times 1800 = 403.2 \text{ ms}$ per array per polarization, already much beyond the targeted maximum sweep duration of 5 ms.

The key realization of our contribution is that we can implement antenna switching instead of beam sweeping, by exploiting the channel select register to switch each antenna ON one at a time, requiring $3.5 \mu\text{s}$ each. It then requires only $3.5 \mu\text{s} \times 64 = 224 \mu\text{s}$ to sweep an array per polarization, 1800 times faster than beam sweeping. Once the antenna responses are measured, switched beams can be synthesized in postprocessing through SBF. Critically, the switched beams can be swept at any angle without changing the channel sweep duration. To expedite the channel sweep, it is broken down into two sequential sweeps, denoted as the T sweep and the R sweep, from which AoD and AoA of channel paths are estimated, respectively.

1) *T Sweep*: The 64 antennas per T array are swept sequentially, meaning that a single code is transmitted per antenna through time multiplexing; the two polarizations per array are swept sequentially in kind, as are the two arrays T_i , $i = 1$ and 2 themselves, requiring $3.5 \mu\text{s} \times 64 \times 2 \times 2 = 896 \mu\text{s}$ in total for the T sweep. Note that we are

interested not only in the co-polarized path gains ($pq = \text{VV}$ and $pq = \text{HH}$) but also in the cross-polarized path gains ($pq = \text{VH}$ and $pq = \text{HV}$). It is to discriminate them that the two polarizations ($p = \text{V}$ and then $p = \text{H}$) must be transmitted in sequence. The two polarizations, however, can be received in parallel: At R, electronic quasi-omnidirectional (QO) beams in both polarizations are synthesized through ABF across the four arrays simultaneously, exploiting all eight channels: the four vertical channels are combined into one channel ($q = \text{V}$) and the four horizontal channels are combined into another ($q = \text{H}$). Crucially, the analog weights to synthesize the QO beams are programmed only once, during the calibration step in Section III-A, and never need to be reprogrammed.

After sampling and correlation, the T sweep yields the antenna response

$$\mathbf{y}^{T_i, pq}(\tau), \quad i = 1 \text{ and } 2 \quad (1)$$

which is a row vector of 64 CIRs, one row per antenna. There are eight vectors $\mathbf{y}^{T_i, pq}(\tau)$ in total, two arrays indexed through i times four polarization pairs indexed through pq .

2) *R Sweep*: The 64 antennas per receiver array R_j , $j = 1, 2, 3$, and 4 are swept sequentially as in the T sweep; however, in contrast to the T sweep, the two polarizations and the four arrays are swept in parallel on the eight receiver channels, requiring $3.5 \mu\text{s} \times 64 = 224 \mu\text{s}$. At T, QO beams are transmitted in V and in H in sequence to capture both the co- and cross-polarization properties, as explained early, so the total R sweep requires $224 \mu\text{s} \times 2 = 448 \mu\text{s}$. After sampling

and correlation, the R sweep yields the antenna response

$$y^{R,pq}(\tau), \quad j = 1, 2, 3, \text{ and } 4. \quad (2)$$

In summary, the channel sweep duration, the T sweep plus the R sweep, requires $896 \mu\text{s} + 448 \mu\text{s} = 1.344 \text{ ms}$, well within the targeted 5 ms. The antennas responses are postprocessed through SBF to extract the channel paths and their properties, as described in Section IV.

Note in passing that while the very recent work in [38] implements antenna switching with actual 28-GHz switched arrays, because all the T antennas and all the R antennas are switched in tandem, the channel sweep duration is very long, equivalent to 114.688 ms if implemented with our system architecture. It is because ours are phased—not switched—arrays that we can also implement ABF to synthesize QO beams and break the total channel sweep down into separate T and R antenna sweeps, reducing it to just 1.344 ms.

E. Mobile Robot and Positioning System

The T section was mounted on a tripod at 2.0 m and the R section was mounted on a mobile robot at 1.6 m, as shown in the hallway environment in Fig. 1(d). The autonomous robot, described in detail in [36], supports rapid data acquisition coupled with a navigational system—laser-guided indoors and military-grade GPS outdoors—that reports its position with centimeter accuracy, its velocity with 1-mm/s precision, and its heading within 1° error. The robot also generates a 2-D map of the environment, providing a global coordinate system against which the AoD and AoA are referenced, to enable the development of map-based channel models through raytracing-assisted modeling [37].

III. SYSTEM CALIBRATION

In this section, we describe the precision calibration techniques developed in house to enable the T and R sweeps, namely, calibration of the analog weights to synthesize QO beams, calibration of the CIR to extend the dynamic range of the system, calibration of the digital weights to synthesize sweepable beams through SBF, and verification that the phase drift in untethered mode is negligible, to enable SBF.

A. Analog Weights

As shown in Section II-A, the analog weight of an array antenna is a complex amplitude defined by a magnitude state (8-bit precision, $2^8 = 256$ possible values) and a phase state (6-bit precision, $2^6 = 64$ possible values), which can be programmed independently. Although each state has a nominal value, the actual values may vary significantly between arrays due to different electrical path lengths and other sources of distortion [22]–[24]. This calls for precision characterization of the state values per antenna per polarization for the two T arrays and four R arrays to design QO beams at both ends.

To that end, a vector network analyzer (VNA) was utilized, for which port 1 of the VNA was connected to a horn antenna and port 2 was connected to the array under inspection. The horn and the array were separated by 3 m—well in their far-field—in an anechoic chamber. Fig. 3 shows a photograph of

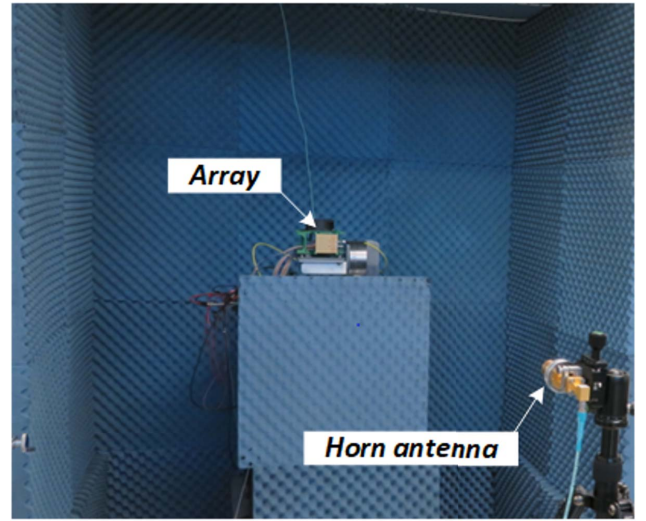


Fig. 3. Calibration of the ABF weights in an anechoic chamber using a VNA connected to a horn antenna on port 1 and the array under inspection on port 2.

the setup. Each antenna was activated one-by-one through the channel select register. The antenna's magnitude state was set to its maximum value because it was found easier to obtain QO beams with equal magnitude, and naturally selecting the maximum value enhanced the link budget. With the magnitude value set, the 64 phase values were cycled through and the corresponding complex weight was recorded as the VNA S_{21} parameter at 28.5 GHz.

With the analog weights characterized, a genetic algorithm was run to design the QO beams, namely to select the optimal set of analog weights per array per polarization— $64 \times 2 \times 2 = 256$ at T and $64 \times 4 \times 2 = 512$ at R—given the 64 possible weight values per antenna. A genetic algorithm was chosen because it provides a good solution to the integer program with reasonable computation time. The objective of the integer program was to maximize the minimum beam gain over the $\pm 45^\circ$ azimuth and $\pm 25^\circ$ elevation FoV per array. The algorithm inputted the nominal 3-D V and H patterns, $G_{\text{MSA}}^{pq}(\theta)$, for the individual MSAs with 1.2-dBi boresight gain, simulated through HFSS [39] by the array designers [23], [24] and shown in Fig. 4(a) and (b). Because of such low mutual coupling between the polarizations ($< -35 \text{ dB}$), the QO beams were designed independently per polarization to reduce computation time. Fig. 4(c) and (d) shows the result of the design: the 3-D QO beam patterns for both polarizations at R for the T sweep, $G_{\text{QO}}^{T,pq}(\theta^R)$, measured in our anechoic chamber with 1° sweep angle within R's FoV. The 3-D QO beam patterns at T for the R sweep (not shown), $G_{\text{QO}}^{R,pq}(\theta^T)$, are similar. All four QO beams have a boresight gain of about 21 dBi.

B. Channel Impulse Response

As shown in Section II-C, the ideal CIR of the system is the autocorrelation of the transmitted PN code. It corresponds to the ideal pulse shown in Fig. 5, with 0.5 ns width (per 2-GHz half-power bandwidth) and 66-dB peak-to-sidelobe ratio (power equivalent of the 33-dB processing gain). The nonidealities of the T and R sections distort the ideal pulse,

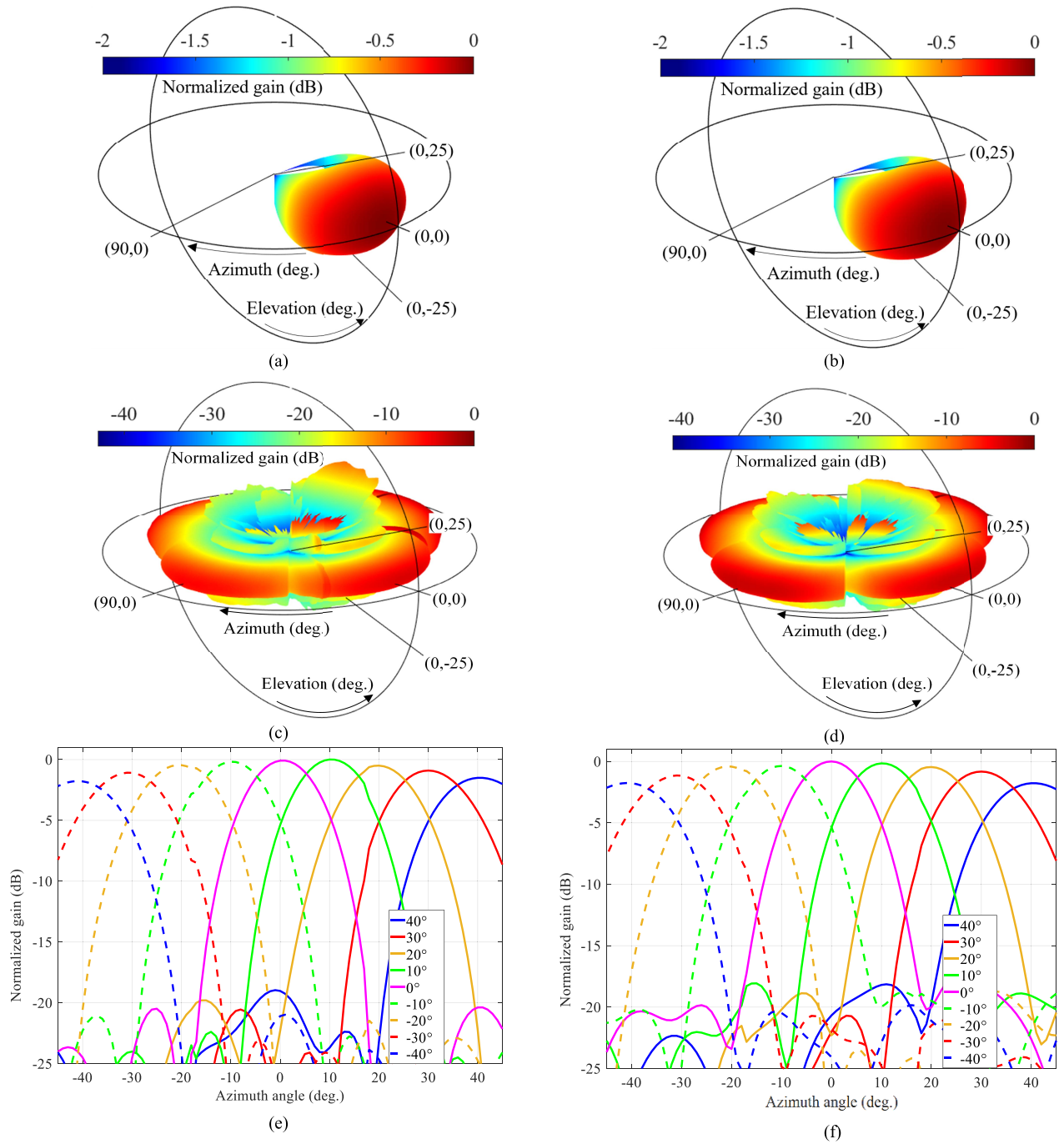


Fig. 4. Receiver antenna patterns in vertical and horizontal polarizations. (a) and (b) 3-D MSAs, simulated. (c) and (d) 3-D QO beams for the T sweep, measured. (e) and (f) 2-D beams swept in azimuth at 10° through SBF for the R sweep, measured. (a), (c), and (e) V polarization. (b), (d), and (f) H polarization.

introducing spurious pulses in the delay profile that, without calibration, could be misclassified as reflections in the wireless channel being sounded. The spurious pulses can be seen as part of the uncalibrated pulse in Fig. 5, measured for some illustrative T-R channel. In our work, calibration is carried out by way of predistortion and postdistortion filtering. Predistortion filtering is preferable because it can be applied in high signal-to-noise conditions at T to avoid boosting the noise level at R, but as we shall see, postdistortion filtering is also required in our application.

Instead of the conventional back-to-back method [40], predistortion filters were designed through an OTA method [30], [41]. The methods are similar in that they both account for the distortion caused by the T and R sections, but the OTA method in addition accounts for the RF components in the SiGe chips on the printed circuit boards, which also distort the CIR but are not accessible through connectors, as required by the back-to-back method. The OTA method mimicked operation in the field, with the T section mounted on the tripod and the R section mounted on the robot. The method exploited the

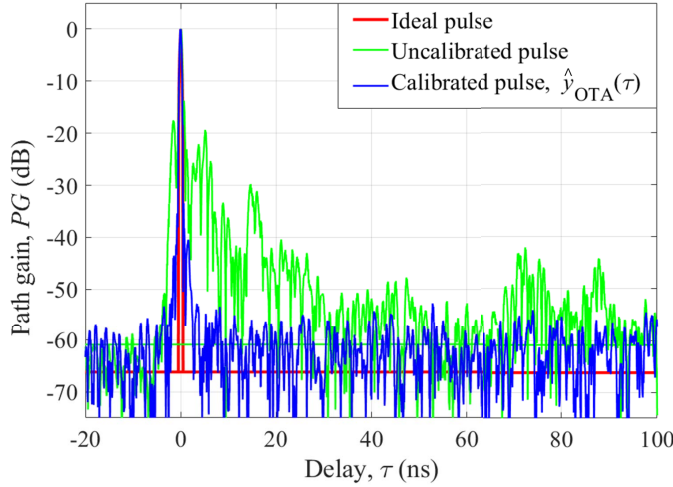


Fig. 5. Calibration of the CIR. The nonidealities of the system hardware distort the ideal pulse (red) into the uncalibrated pulse (green), measured for some illustrative T-R channel. Calibration extended the peak-to-sidelobe ratio from 18 to 55 dB.

line-of-sight (LoS) path between any pair of T and R arrays under inspection. Specifically, the two arrays were pointed toward each other with their normals aligned, again separated 3 m in the anechoic chamber. First, the ideal PN code was transmitted on a T channel and the code distorted by the system was received on an R channel. The received code was then normalized: its correlation pulse was translated to 0-ns delay and scaled to 0-dB path gain to remove the properties of the LoS path. The normalized code was subsequently deconvolved from the ideal code, yielding the predistorted code. It follows that when transmitting the predistorted code in place of the ideal code, the code that is received is ideal. Fig. 5 shows the calibrated OTA pulse, $\hat{y}_{\text{OTA}}(\tau)$. Predistortion filtering reduced the spurious pulses in the uncalibrated pulse from -18 to -55 dB, extending the dynamic range by 27 dB.

As described in Section II-D, the code transmitted on a T channel is received by all eight R channels since they are sampled simultaneously. Accordingly, to design the predistorted codes, one of eight channels was chosen arbitrarily as the reference R channel. However, the predistorted code then only accounts for the nonidealities between the T channel and the reference R channel and not for the residual nonidealities between the reference R channel and the other seven R channels. To bridge the gap, a unique postdistorted code was designed for each of the other seven R channels. Specifically, the same OTA setup for the predistortion design was used for the postdistortion design, except that the reference R channel was swapped round robin with the other seven R channels. The predistorted code was transmitted and the code distorted by the system was received on the other R channels. The received code was then normalized, yielding the postdistorted code. It follows that deconvolving the postdistorted code from the predistorted code that is received yields the ideal code. Details of the postdistortion design can be found in [42].

For the T sweep, a unique predistorted code was designed between the T channel of each antenna per array per polarization and the reference R channel, for a total of

$64 \times 2 \times 2 = 256$ predistorted codes. For each predistorted code, seven postdistortion codes were designed, for a total of $256 \times 7 = 1792$ postdistorted codes. Altogether, $256 + 1792 = 2048$ codes were necessary to measure the calibrated antenna responses $\hat{y}^{\text{T},pq}(\tau)$. Such a large number clearly required fully automating processing aside from the mechanical alignment of the arrays in using a 3-D rotator. Analogously, for the R sweep, a unique predistorted code was designed between the T channel of the QO beam synthesized across both arrays per polarization and each array antenna of the reference R channel, for a total of $2 \times 64 = 128$ predistorted codes. For each predistorted code, seven postdistortion codes were designed, for a total of $128 \times 7 = 896$ postdistorted codes. Altogether, $128 + 896 = 1024$ codes were necessary to measure the calibrated antenna responses $\hat{y}^{\text{R},pq}(\tau)$.

C. Digital Weights

As in ABF, SBF is implemented by applying complex weights to the array antennas—specifically to the antenna responses—to synthesize beams in postprocessing. The ideal digital weights for array T_i steered toward θ^{T} and array R_j steered toward θ^{R} are [43]

$$\begin{aligned} s^{\text{T}_i}(\theta^{\text{T}}) &= e^{j \frac{2\pi}{\lambda} (\cos \theta^{\text{T},\text{A}} \cdot \cos \theta^{\text{T},\text{E}}, \sin \theta^{\text{T},\text{A}} \cdot \cos \theta^{\text{T},\text{E}}, \sin \theta^{\text{T},\text{E}})} \cdot X^{\text{T}_i} \\ s^{\text{R}_j}(\theta^{\text{R}}) &= e^{j \frac{2\pi}{\lambda} (\cos \theta^{\text{R},\text{A}} \cdot \cos \theta^{\text{R},\text{E}}, \sin \theta^{\text{R},\text{A}} \cdot \cos \theta^{\text{R},\text{E}}, \sin \theta^{\text{R},\text{E}})} \cdot X^{\text{R}_j}. \end{aligned} \quad (3)$$

The weights are stored compactly as 64-length row vectors (typically referred to as steering vectors), where X^{T_i} and X^{R_j} are 3×64 matrices of the 3-D positions of the array antennas as mounted on the tripod and on the robot, and θ^{T} , θ^{R} , X^{T_i} , and X^{R_j} are referenced to the global coordinate system of the environment mapped by the robot, as described in Section II-E.

Recall from Section III-A that the antennas already have fixed analog weights programmed to synthesize QO beams. Therefore, the ideal digital weights cannot be directly applied. Furthermore, the predistorted and postdistorted codes inherent to the calibrated antenna responses must also be considered. To that end, the OTA method in Section III-B was exploited to calibrate both factors out in a single step since both factors were captured in the calibrated OTA responses ($\hat{y}_{\text{OTA}}^{\text{T},pq}(\tau)$, $\hat{y}_{\text{OTA}}^{\text{R},pq}(\tau)$). The total process is shown as a flow-chart in Fig. 6. The additional benefit of the OTA method is that the ideal digital weights ($s^{\text{T}_i}(\theta_{\text{LoS}}^{\text{T}})$, $s^{\text{R}_j}(\theta_{\text{LoS}}^{\text{R}})$) were given directly from the geometry of the setup through the ground-truth angle of the LoS path $\theta_{\text{LoS}} = (\theta_{\text{LoS}}^{\text{T}}, \theta_{\text{LoS}}^{\text{R}})$.

Accordingly, the calibrated digital weights follow as

$$\begin{aligned} \hat{s}^{\text{T}_i,pq}(\theta^{\text{T}}) &= \mathbf{w} \odot s^{\text{T}_i}(\theta^{\text{T}}) \odot s^{\text{T}_i}(\theta_{\text{LoS}}^{\text{T}}) \oslash \hat{y}_{\text{OTA}}^{\text{T}_i,pq}(\tau = 0) \\ \hat{s}^{\text{R}_j,pq}(\theta^{\text{R}}) &= \mathbf{w} \odot s^{\text{R}_j}(\theta^{\text{R}}) \odot s^{\text{R}_j}(\theta_{\text{LoS}}^{\text{R}}) \oslash \hat{y}_{\text{OTA}}^{\text{R}_j,pq}(\tau = 0) \end{aligned} \quad (4)$$

where \odot and \oslash denote the Hadamard multiplication and division operators, respectively. The ideal weights were calibrated through the difference (ratio) between the ideal OTA weights and the calibrated OTA weights [the pulse value at its peak, $\hat{y}_{\text{OTA}}(\tau = 0)$], yielding the calibrated

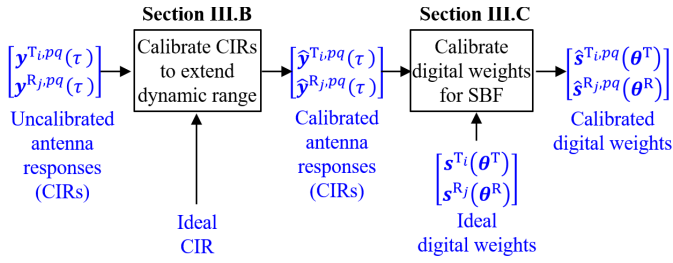


Fig. 6. Calibration of the digital weights, displayed as a flowchart.

weights. It follows that when the calibrated antenna responses ($\hat{\mathbf{y}}^{T_i,pq}(\tau)$, $\hat{\mathbf{y}}^{R_j,pq}(\tau)$) are beamformed through the calibrated weights ($\hat{\mathbf{s}}^{T_i,pq}(\theta^T)$, $\hat{\mathbf{s}}^{R_j,pq}(\theta^R)$), it is equivalent to beamforming the ideal antenna responses through the ideal weights. Note that because the calibrated responses are polarization dependent, so too are the calibrated weights.

The Kaiser taper window w [44] was applied in (4) to suppress the beam sidelobes at the expense of widening the main lobe. The Kaiser window was chosen because it has a tunable parameter β to balance the two factors. A value of $\beta = 2.12$ was found empirically to achieve a favorable balance, theoretically enhancing suppression of the first lobe from 12.8 to 21.1 dB while widening the azimuth beamwidth from 13.8° to 15.6°, and the elevation beamwidth from 10.6° to 12.6°. Fig. 4(e) and (f) shows the measured SBF beams for both polarizations at R, steered in azimuth for a nominal elevation angle of 0°. The beams were generated through the OTA setup, however, by mechanically rotating the R array every 10° and electronically steering the beam back to alignment with the LoS path from the T array through SBF.

While reducing the channel sweep duration by orders of magnitude is a significant advantage of our SBF approach, the other significant advantage is the accuracy that comes from the effectively infinite precision of digital weights compared to the 8-bit magnitude and 6-bit phase precision of the analog weights. This is what enables beam sweeping at any angle, pivotal to the successful implementation of super-resolution algorithms such as CLEAN [10], [45], MUSIC [46], ESPRIT [47], SAGE [48], [49], and RiMAX [50]. Yet, where infinite precision matters most is in the fine calibration of the digital weights coupled with fine window tapering for sidelobe suppression, which together were able to synthesize the ideal beams patterns shown in Fig. 4(e) and (f). All these features are essential to realizing real-time channel sounding with subdegree angle estimation, as we shall see later.

D. Phase Drift

A condition necessary to the operation of our system is that the phase drift between the T and R LOs be negligible during the sweep of the 64 antennas per array per polarization, over which SBF takes place. As described in Section II-B, the LOs rely on untethered Rubidium clocks at each end for discipline. The time drift rate between the two clocks is spec'd and was confirmed through our measurement as 2 ns/min at worst [30], [42], equivalent to 342°/s in phase

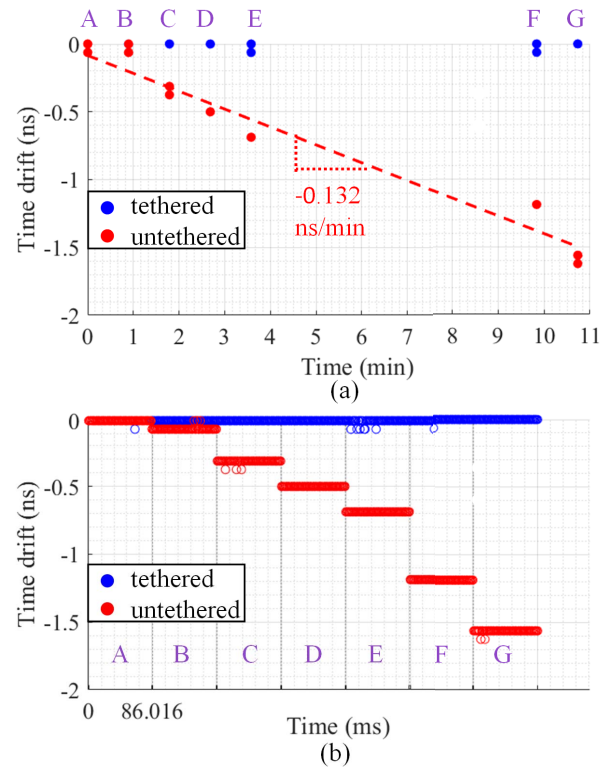


Fig. 7. Comparison of the time drift between untethered mode (red) with free-running LOs at T and R, and tethered mode (blue) with one local LO distributed through an optical cable. (a) Large-scale drift over seven bursts (A-G) of channel sweeps captured minutes apart was fit to 0.132 ns/min. (b) Small-scale drift over each burst of 64 consecutive channel sweeps ($64 \times 1.344 \text{ ms} = 86.016 \text{ ms}$) was undetectable.

drift rate at 28.5 GHz. The sweep duration per array per polarization is 224 μs per Section II-D, over which the spec'd phase drift is 0.08° at worst. This is orders of magnitude smaller than the standard deviation of the LO's phase noise, reported in [30] as 5.4°. Fig. 7 compares the time drift between (normal) untethered mode with free-running LOs at T and R, and (controlled) tethered mode with one local LO distributed through an optical cable. The large-scale time drift over seven bursts (A-G) of channel sweeps captured minutes apart was fit to 0.132 ns/min. Yet, the small-scale time drift over each burst of 64 consecutive channel sweeps ($64 \times 1.344 \text{ ms} = 86.016 \text{ ms}$) was undetectable.

IV. CHANNEL PATH PROPERTIES

In this section, we describe how the measured antenna responses are beamformed into power-angle delay profiles, from which the channel paths and the properties of each path are extracted.

A. Switched Beamforming

The first step in extracting the channel paths is to generate power-angle delay profiles, whose peaks correspond to distinct paths. The power-AoD delay profiles (PDDPs) $p^{T_i,pq}(\theta^T, \tau)$ and power-AoA delay profiles (PADPs) $p^{R_j,pq}(\theta^R, \tau)$ are generated from the calibrated antenna responses $\hat{\mathbf{y}}^{T_i,pq}(\tau)$ and

$\hat{\mathbf{y}}^{R_j,pq}(\tau)$, respectively. Specifically, the digital weights are applied to the responses to synthesize beams that are swept in $\boldsymbol{\theta}^T$ and $\boldsymbol{\theta}^R$ as

$$\begin{aligned} p^{T_i,pq}(\boldsymbol{\theta}^T, \tau) &= |\hat{s}^{T_i,pq}(\boldsymbol{\theta}^T) \cdot \hat{\mathbf{y}}^{T_i,pq}(\tau)^\dagger|^2 \\ p^{R_j,pq}(\boldsymbol{\theta}^R, \tau) &= |\hat{s}^{R_j,pq}(\boldsymbol{\theta}^R) \cdot \hat{\mathbf{y}}^{R_j,pq}(\tau)^\dagger|^2 \end{aligned} \quad (5)$$

where \dagger denotes the Hermitian. Since our objective is to obtain subdegree angle error, the beams are swept at 1° , which corresponds to the sampling interval of $\boldsymbol{\theta}^T$ and $\boldsymbol{\theta}^R$. Since each array only has $\pm 45^\circ$ azimuth FoV, $p^{T_i,pq}(\boldsymbol{\theta}^T, \tau)$, $i = 1$ and 2 are stitched together into a composite PDDP to extend the AoD azimuth FoV to $\pm 90^\circ$; likewise, $p^{R_j,pq}(\boldsymbol{\theta}^R, \tau)$, $j = 1, 2, 3$, and 4 are stitched together into a composite PADP to extend the AoA azimuth FoV to $\pm 180^\circ$. The sampling interval of τ is 62.5 ps, which is the inverse of the 16-GHz sampling rate.

Note that while the $10 \cdot \log_{10} 64 = 18$ dB coherence gain from beam sweeping through ABF is initially lost by antenna switching instead, the coherence gain is recovered when synthesizing beams across the antennas through SBF; this is true even if the antenna responses initially fall below the noise floor.

The equations in (5) correspond to narrowband beamforming, which as a rule of thumb can be applied when the bandwidth is less than 10% of the center frequency, as in our application. For applications in which the narrowband assumption does not hold, wideband beamforming can be applied instead, for example, by transmitting an orthogonal frequency-division multiplexing (OFDM) waveform instead of a PN code. The weights would then be frequency dependent. For example, the maximum delay window of our PN code ($2047 \text{ chips} \times 0.5 \text{ ns/chip} = 1023.5 \text{ ns}$) is equivalent to a subcarrier spacing of $1/1023.5 \text{ ns} = 977.2 \text{ MHz}$. In practice, it is possible to obtain frequency-dependent weights with this precision only through SBF.

B. Path Extraction

The conventional approach to extracting channel paths is to search over the PDDPs/PADPs and identify peaks as distinct paths. Instead, we adopted the SAGE super-resolution algorithm [49], which delivers angle and delay resolution beyond that inherent to the respective beamwidth and bandwidth of the system. Essentially, it interpolates in between the angle and delay samples of the PDDPs/PADPs based on the calibrated beam patterns [see Fig. 4(e) and (f)] and calibrated CIR (Fig. 5) of the system, respectively. To do this effectively, the beam patterns and CIR must be well behaved, *i.e.*, have a single peak within the main lobe and within the main pulse, respectively. The calibration techniques described earlier ensure that this is true.

Note that according to electromagnetic theory [51], path gain is polarization dependent, while the geometrical properties of the paths, namely angle and delay, are not. The theory is applied to our path extraction algorithm by running SAGE on the product of the four composite PDDPs ($pq = \text{VV, VH, HV, and HH}$) and on the product of the four composite PADPs. This ensures that all four polarizations have the same angle

and delay, mitigating the angle and delay estimation error per polarization to boot.

C. Path Correspondence

The number of paths extracted from the PDDPs and the PADPs should be equal since, in principle, the channel during the respective T and R sweeps is the same. To ensure compliance, the PDDPs and PADPs cannot simply be summed as over the four polarizations in Section IV-B since they have different domains, $(\boldsymbol{\theta}^T, \tau)$ and $(\boldsymbol{\theta}^R, \tau)$. Rather, we resort to the assignment problem [52], which finds a one-to-one correspondence between the two sets of extracted paths, by minimizing the difference in the path properties between corresponding pairs. The assignment problem was selected due to its robustness, in that it minimizes the difference across all corresponding pairs jointly, versus a greedy approach that minimizes the difference per pair independently and can thus yield a many-to-one correspondence. The properties employed for correspondence are the five properties that the PDDPs and PADPs share, namely $[\text{PG}_n^{\text{VV}}, \text{PG}_n^{\text{VH}}, \text{PG}_n^{\text{HV}}, \text{PG}_n^{\text{HH}}]$ and τ_n . The difference per pair is composed over the five properties as the sum of the absolute difference per property. Because path gain and delay have different units and scales, they are first normalized² before summing.

What's more, the directional antenna patterns of the T and R sweeps are embedded in the PDDPs and PADPs. The patterns are composed from the SBF, MSA, and QO gains at both ends and so are expressed as a function of double-directional angle $(\boldsymbol{\theta}^T, \boldsymbol{\theta}^R)$ as

$$\begin{aligned} G^{T_i,pq}(\boldsymbol{\theta}^T, \boldsymbol{\theta}^R) &= \overbrace{\hat{s}^{T_i,pq}(\boldsymbol{\theta}^T) \cdot G_{\text{MSA}}^{pq}(\boldsymbol{\theta}^T) \cdot G_{\text{QO}}^{T,pq}(\boldsymbol{\theta}^R)}^{\text{SBF}} \\ G^{R_j,pq}(\boldsymbol{\theta}^T, \boldsymbol{\theta}^R) &= \underbrace{\hat{s}^{R_j,pq}(\boldsymbol{\theta}^R) \cdot G_{\text{MSA}}^{pq}(\boldsymbol{\theta}^R) \cdot G_{\text{QO}}^{R,pq}(\boldsymbol{\theta}^T)}_{\text{SBF}}. \end{aligned} \quad (6)$$

Thus, for the path gains to correspond between the PDDPs and PADPs, $G^{T_i,pq}(\boldsymbol{\theta}^T, \boldsymbol{\theta}^R)$ and $G^{R_j,pq}(\boldsymbol{\theta}^T, \boldsymbol{\theta}^R)$ are deemed as part of the correspondence process. Thanks to calibration and antenna deembedment, the path properties extracted represent the “pristine” response of the channel alone and not that of the measurement system.

Once the one-to-one correspondence is found, the final values of $(\theta_n^{T,A}, \theta_n^{T,E})$ and $(\theta_n^{R,A}, \theta_n^{R,E})$ are given directly from the respective PDDPs and PADPs of corresponding pair n , whereas the final values of the shared properties $(\text{PG}_n^{\text{VV}}, \text{PG}_n^{\text{VH}}, \text{PG}_n^{\text{HV}}, \text{PG}_n^{\text{HH}})$ and τ_n are averaged over the corresponding pair.

Although it was not implemented here, the Doppler frequency shift of each path, Δf_n , can also be extracted given the real-time operation of the channel sounder, up to a maximum shift of $(1/2\Delta t) = 384.6 \text{ kHz}$ [53], where $\Delta t = 1.3 \text{ ms}$ is the channel sweep duration.

V. ILLUSTRATIVE RESULTS

This section presents the results collected from field measurements to illustrate the capabilities of the system.

²The normalization procedure is described in [37].

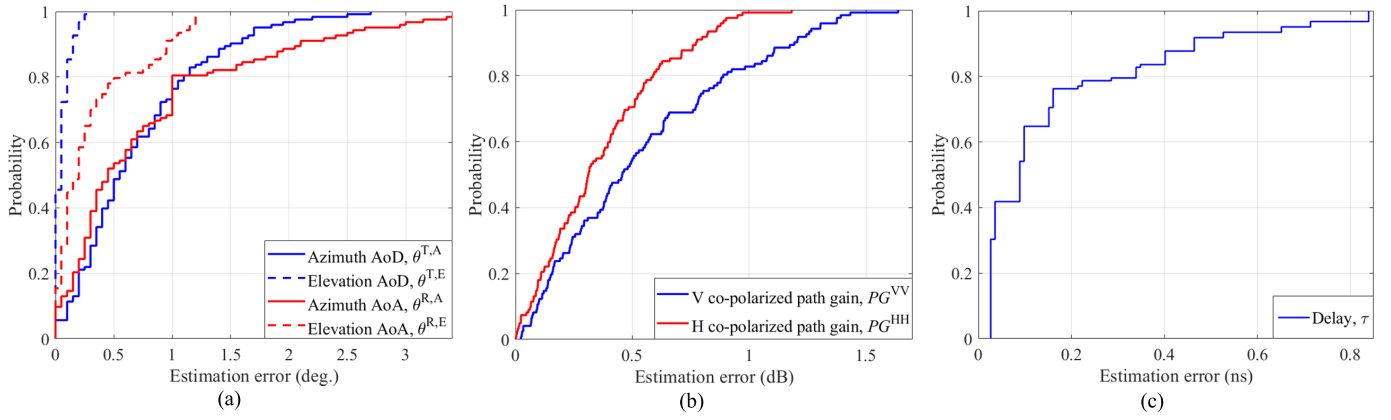


Fig. 8. CDF of estimation error in path properties. (a) 3-D double-directional angle. (b) Co-polarized path gain. (c) Delay.

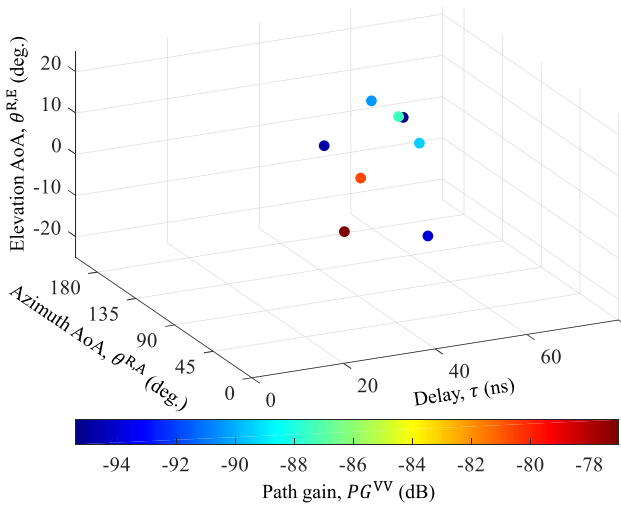


Fig. 9. Multiple paths extracted from a single measurement in our laboratory, displayed in the domain of four ($[\theta_n^{R,A}, \theta_n^{R,E}, PG_n^{VV}, \tau_n]$) out of nine path properties extracted.

To gauge its accuracy in estimating the path properties, a total of 266 measurements were collected in our laboratory, with varying T and R positions to exhaust the full 3-D double-directional FoV of the system. The estimation error was quantified against the LoS path, whose ground-truth properties were given from the known geometry of T and R. Fig. 8 shows the cumulative distribution functions (CDFs) of the estimation error in 3-D double-directional angle, co-polarized path gain³, and delay, aggregated across the 266 measurements, reporting an average error of 0.47° in angle (over the four angles), 0.48 dB in path gain (over the two copolarized path gains), and 0.18 ns in delay. Of course, the system is capable of extracting the properties of all channel paths, not just the LoS path. In fact, Fig. 9 shows an illustrative plot of the properties of eight paths extracted from a single measurement in our laboratory.

The transmit power was set to about 9 dBm so that when added to the 21-dBi boresight gain of the measured QO beams, the effective isotropic radiated power (EIRP) was

³The cross-polarized path gains ($pq = VH$ and HV) of the LoS path are theoretically zero. In fact, they went undetected in our measurements and so were not reported here.

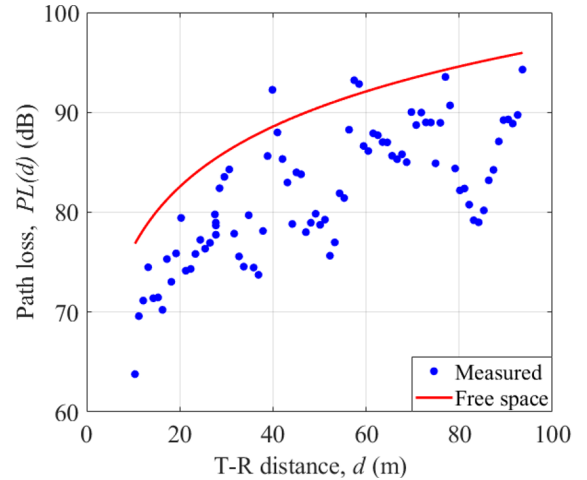


Fig. 10. Path loss versus distance collected for 85 T-R locations in the hallway environment. The path loss of all paths extracted plotted and against the theoretical free space path loss. The waveguiding in the hallway caused the path loss to fall short of free space.

measured as 30 dBm with a spectrum analyzer. Together with 37.8-dB processing gain, 18-dB coherence gain, and other factors of the link budget such as single antenna gain, LNA gain, noise floor and noise factor, and cable loss, the maximum measureable path loss for the R sweep was 136.4 dB (and was comparably valued for the T sweep). Fig. 10 shows path loss versus distance collected for 85 T-R locations in the hallway environment. The path loss for the T-R location at distance d was computed over all paths and polarizations as

$$PL(d) = \frac{0.5}{\sum_n PG_n^{VV}(d) + PG_n^{VH}(d) + PG_n^{HV}(d) + PG_n^{HH}(d)}. \quad (7)$$

The theoretical free-space path loss is also displayed. Waveguiding in the hallway caused the path loss to fall short of free space.

VI. CONCLUSION

In this article, we demonstrated the feasibility of implementing SBF with phased-array antennas. Specifically, instead of sweeping electronic beams synthesized by programming the analog weights of the antennas—also known as ABF, what the

arrays were designed for—we switched through all the antennas and synthesized beams in postprocessing through digital weights. By circumventing the time-consuming programming, we were able to realize a 3-D double-omnidirectional sweep with multiple 28.5-GHz, dual-polarized, 8×8 phased-array antennas at the transmitter and receiver in just 1.3 ms. Furthermore, we were able to synthesize ideal beam patterns due to the effectively infinite precision of digital weights (versus the coarse precision of analog weights), which enabled fine weight calibration for the nonidealities of the system hardware and fine window tapering to suppress sidelobes, translating into average angle estimation error of only 0.47° , as substantiated by field measurements.

REFERENCES

- [1] H. Hashemi, "The indoor radio propagation channel," *Proc. IEEE*, vol. 81, no. 7, pp. 943–968, Jul. 1993.
- [2] C. Gentile *et al.*, "Methodology for benchmarking radio-frequency channel sounders through a system model," *IEEE Trans. Wireless Commun.*, vol. 19, no. 10, pp. 6504–6519, Oct. 2020.
- [3] H. Sawada, H. Nakase, S. Kato, M. Umehira, K. Sato, and H. Harada, "Impulse response model and parameters for indoor channel modeling at 60 GHz," in *Proc. IEEE 71st Veh. Technol. Conf.*, May 2010, pp. 1–5.
- [4] S. Hur, Y.-J. Cho, J. Lee, N.-G. Kang, J. Park, and H. Bann, "Synchronous channel sounder using horn antenna and indoor measurements on 28 GHz," in *Proc. IEEE Int. Black Sea Conf. Commun. Netw. (BlackSeaCom)*, May 2014, pp. 1–5.
- [5] M. R. Akdeniz *et al.*, "Millimeter wave channel modeling and cellular capacity evaluation," *IEEE J. Sel. Areas Commun.*, vol. 32, no. 6, pp. 1164–1179, Jun. 2014.
- [6] J. J. Park *et al.*, "Millimeter-wave channel model parameters for urban microcellular environment based on 28 and 38 GHz measurements," in *Proc. IEEE 27th Annu. Int. Symp. Pers., Indoor, Mobile Radio Commun. (PIMRC)*, Sep. 2016, pp. 1–5.
- [7] D. Dupleich *et al.*, "Directional characterization of the 60 GHz indoor-office channel," in *Proc. 31th URSI Gen. Assem. Sci. Symp. (URSI GASS)*, Aug. 2014, pp. 1–4.
- [8] D. Dupleich, J. Luo, S. Haefner, R. Mueller, C. Schneider, and R. Thomae, "A hybrid polarimetric wide-band beam-former architecture for 5G mm-wave communications," in *Proc. 20th Int. ITG Workshop Smart Antennas*, Mar. 2016, pp. 1–8.
- [9] G. R. MacCartney and T. S. Rappaport, "A flexible millimeter-wave channel sounder with absolute timing," *IEEE J. Sel. Areas Commun.*, vol. 35, no. 6, pp. 1402–1418, Jun. 2017.
- [10] M. Kim, T. Iwata, S. Sasaki, and J.-I. Takada, "Millimeter-wave radio channel characterization using multi-dimensional sub-grid CLEAN algorithm," *IEICE Trans. Commun.*, vol. E103.B, no. 7, pp. 767–779, Jul. 2020.
- [11] B. N. Liya and D. G. Michelson, "Characterization of multipath persistence in device-to-device scenarios at 30 GHz," in *Proc. IEEE Global Commun. Conf.*, Dec. 2016, pp. 1–6.
- [12] A. Maltsev, R. Maslennikov, A. Sevastyanov, A. Khoryaev, and A. Lomayev, "Experimental investigations of 60 GHz WLAN systems in office environment," *IEEE J. Sel. Areas Commun.*, vol. 27, no. 8, pp. 1488–1499, Oct. 2009.
- [13] A. W. Mbugua, W. Fan, Y. Ji, and G. F. Pedersen, "Millimeter wave multi-user performance evaluation based on measured channels with virtual antenna array channel sounder," *IEEE Access*, vol. 6, pp. 12318–12326, 2018.
- [14] A. J. Weiss *et al.*, "Configuration and control of a millimeter-wave synthetic aperture measurement system with uncertainties," in *Proc. 95th ARFTG Microw. Meas. Conf. (ARFTG)*, Aug. 2020, pp. 1–4.
- [15] *IEEE 802.11ay Standard*. Accessed: Aug. 2021. [Online]. Available: https://www.ieee802.org/11/Reports/tgay_update.htm
- [16] A. Hughes, "Measuring the impact of beamwidth on the correlation distance of 60 GHz indoor and outdoor channels," *IEEE Open J. Veh. Technol.*, vol. 2, pp. 180–193, 2021.
- [17] B. Rupakula, A. Nafe, S. Zahir, Y. Wang, T.-W. Lin, and G. Rebeiz, "63.5–65.5-GHz transmit/receive phased-array communication link with 0.5–2 Gb/s at 100–800 m and $\pm 50^\circ$ scan angles," *IEEE Trans. Microw. Theory Techn.*, vol. 66, no. 9, pp. 1–13, Sep. 2018.
- [18] X. Gu *et al.*, "Development, implementation, and characterization of a 64-element dual-polarized phased-array antenna module for 28-GHz high-speed data communications," *IEEE Trans. Microw. Theory Techn.*, vol. 67, no. 7, pp. 2975–2984, Jul. 2019.
- [19] C.-N. Chen *et al.*, "38-GHz phased array transmitter and receiver based on scalable phased array modules with endfire antenna arrays for 5G MMW data links," *IEEE Trans. Microw. Theory Techn.*, vol. 69, no. 1, pp. 980–999, Jan. 2021.
- [20] Y. Wang, H. Chung, Q. Ma, and G. M. Rebeiz, "A 57.5–65.5 GHz phased-array transmit beamformer in 45 nm CMOS SOI with 5 dBm and 6.1% linear PAE for 400 MBaud 64-QAM waveforms," *IEEE Trans. Microw. Theory Techn.*, vol. 69, no. 3, pp. 1772–1779, Mar. 2021.
- [21] L. Gao and G. M. Rebeiz, "A 22–44-GHz phased-array receive beamformer in 45-nm CMOS SOI for 5G applications with 3–3.6-dB NF," *IEEE Trans. Microw. Theory Techn.*, vol. 68, no. 11, pp. 4765–4774, Nov. 2020.
- [22] Q. Ma, H. Chung, Y. Yin, T. Kanar, S. Zahir, and G. M. Rebeiz, "A 5G 24–30 GHz 2×32 element dual-polarized dual-beam phased array base-station for 2×2 MIMO system," in *Proc. IEEE Global Commun. Conf. (GLOBECOM)*, Dec. 2019, pp. 1–5.
- [23] A. Nafe, M. Sayginer, K. Kibaroglu, and G. M. Rebeiz, " 2×64 dual-polarized dual-beam single-aperture 28 GHz phased array with high cross-polarization rejection for 5G polarization MIMO," in *IEEE MTT-S Int. Microw. Symp. Dig.*, Jun. 2019, pp. 484–487.
- [24] A. Nafe, M. Sayginer, K. Kibaroglu, and G. M. Rebeiz, " 2×64 -element dual-polarized dual-beam single-aperture 28-GHz phased array with 2×30 Gb/s links for 5G polarization MIMO," *IEEE Trans. Microw. Theory Techn.*, vol. 68, no. 9, pp. 3872–3884, Sep. 2020.
- [25] R. Wang *et al.*, "Stationarity region of mm-wave channel based on outdoor microcellular measurements at 28 GHz," in *Proc. MILCOM IEEE Mil. Commun. Conf. (MILCOM)*, Oct. 2017, pp. 782–787.
- [26] C. U. Bas *et al.*, "Real-time millimeter-wave MIMO channel sounder for dynamic directional measurements," *IEEE Trans. Veh. Technol.*, vol. 68, no. 9, pp. 8775–8789, Sep. 2019.
- [27] A. Chopra, A. Thornburg, O. Kanhere, A. Termos, S. S. Ghassemzadeh, and T. S. Rappaport, "Real-time millimeter wave omnidirectional channel sounder using phased array antennas," 2020, *arXiv:2009.11093*. [Online]. Available: <http://arxiv.org/abs/2009.11093>
- [28] O. Ozdemir, F. Erden, I. Guvenc, T. Yekan, and T. Zarian, "28 GHz mmWave channel measurements: A comparison of horn and phased array antennas and coverage enhancement using passive and active repeaters," 2020, *arXiv:2002.00121*. [Online]. Available: <http://arxiv.org/abs/2002.00121>
- [29] P. Papazian, D. Caudill, C. Gentile, J. Chuang, and N. Golmie, "62.5-GHz phased-array channel sounder for double-directional angle estimation," in *Proc. 13th Eur. Conf. Antennas Propag. (EuCAP)*, Mar. 2019, pp. 1–9.
- [30] D. Caudill, P. B. Papazian, C. Gentile, J. Chuang, and N. Golmie, "Omnidirectional channel sounder with phased-ArrayAntennas for 5G mobile communications," *IEEE Trans. Microw. Theory Techn.*, vol. 67, no. 7, pp. 2936–2945, Jul. 2019.
- [31] C. Slezak, A. Dhananjay, and S. Rangan, "60 GHz blockage study using phased arrays," in *Proc. 51st Asilomar Conf. Signals, Syst., Comput.*, Oct. 2017, pp. 1655–1659.
- [32] C. Slezak, V. Semkin, S. Andreev, Y. Koucheryavy, and S. Rangan, "Empirical effects of dynamic human-body blockage in 60 GHz communications," *IEEE Commun. Mag.*, vol. 56, no. 12, pp. 60–66, Dec. 2018.
- [33] R. J. Weiler *et al.*, "Millimeter-wave outdoor access shadowing mitigation using beamforming arrays," in *Proc. 10th Eur. Conf. Antennas Propag. (EuCAP)*, Apr. 2016, pp. 1–5.
- [34] B. De Beelde, E. Tanghe, M. Yusuf, D. Plets, E. De Poorter, and W. Joseph, "60 GHz path loss modelling inside ships," in *Proc. 14th Eur. Conf. Antennas Propag. (EuCAP)*, Mar. 2020, pp. 1–5.
- [35] S. G. Sanchez, S. Mohanti, D. Jaishighani, and K. R. Chowdhury, "Millimeter-wave base stations in the sky: An experimental study of UAV-to-ground communications," *IEEE Trans. Mobile Comput.*, early access, Aug. 3, 2020, doi: [10.1109/TMC.2020.3013575](https://doi.org/10.1109/TMC.2020.3013575).
- [36] P. B. Papazian, K. A. Remley, C. Gentile, and N. Golmie, "A radio channel sounder for mobile millimeter-wave communications: System implementation and measurement assessment," *IEEE Trans. Microw. Theory Techn.*, vol. 64, no. 9, pp. 2924–2932, Sep. 2016.
- [37] C. Lai, R. Sun, C. Gentile, P. B. Papazian, J. Wang, and J. Senic, "Methodology for multipath-component tracking in millimeter-wave channel modeling," *IEEE Trans. Antennas Propag.*, vol. 67, no. 3, pp. 1826–1836, Mar. 2019.

- [38] *5G Smart Manufacturing Project*. Accessed: 2021. [Online]. Available: <https://5gsmart.eu/wp-content/uploads/5G-SMART-D4.2-v1.0.pdf>
- [39] *Ansys High-Frequency Structure Simulator (HFSS)*. Accessed: Aug. 2021. [Online]. Available: <https://www.ansys.com/products/electronics/ansys-hfss>
- [40] R. Sun *et al.*, "Design and calibration of a double-directional 60 GHz channel sounder for multipath component tracking," in *Proc. 11th Eur. Conf. Antennas Propag. (EUCAP)*, Mar. 2017, pp. 3336–3340.
- [41] S. Y. Jun, D. Caudill, J. Senic, C. Gentile, J. Chuang, and N. Golmie, "Over-the-air calibration of a dual-beam dual-polarized 28-GHz phased-array channel sounder," in *Proc. IEEE Int. Symp. Antennas Propag. North Amer. Radio Sci. Meeting*, Jul. 2020, pp. 1093–1094.
- [42] P. B. Papazian *et al.*, "Calibration of millimeter-wave channel sounders for super-resolution multipath component extraction," in *Proc. 10th Eur. Conf. Antennas Propag. (EuCAP)*, Apr. 2016, pp. 1–5.
- [43] D. K. Cheng, *Fundamentals of Engineering Electromagnetics*. Upper Saddle River, NJ, USA: Prentice-Hall, 1993.
- [44] A. V. Oppenheim, *Discrete-Time Signal Processing*. London, U.K.: Pearson, 1999.
- [45] J. Högbom, "Aperture synthesis with a non-regular distribution of interferometer baselines," *Astron. Astrophys. Suppl. Ser.*, vol. 15, p. 417, Jun. 1974.
- [46] R. O. Schmidt, "Multiple emitter location and signal parameter estimation," *IEEE Trans. Antennas Propag.*, vol. AP-34, no. 3, pp. 276–280, Mar. 1986.
- [47] R. Roy and T. Kailath, "Esprit-estimation of signal parameters via rotational invariance techniques," *IEEE Trans. Acoust., Speech, Signal Process.*, vol. 37, no. 7, pp. 984–995, Jul. 1989.
- [48] J. A. Fessler and A. O. Hero, "Space-alternating generalized expectation-maximization algorithm," *IEEE Trans. Signal Process.*, vol. 42, no. 10, pp. 2664–2677, Oct. 1994.
- [49] K. Hausmair, "SAGE algorithm for UWB channel parameter estimation," in *Proc. COST Manage. Committee Meeting*, 2010, pp. 1–7.
- [50] A. Richter, *Estimation of Radio Channel Parameters: Models and Algorithms*. Ilmenau, Germany: ISLE Steuerungstechnik und Leistungselektronik, 2005.
- [51] M. Born and E. Wolf, *Principles of Optics: Electromagnetic Theory of Propagation, Interference and Diffraction of Light*. Amsterdam, The Netherlands: Elsevier, 2013.
- [52] M. S. Bazaraa, J. J. Jarvis, and H. D. Sherali, *Linear Programming and Network Flows*. Hoboken, NJ, USA: Wiley, 2008.
- [53] J. Wang, C. Gentile, P. B. Papazian, J.-K. Choi, and J. Senic, "Quasi-deterministic model for Doppler spread in millimeter-wave communication systems," *IEEE Antennas Wireless Propag. Lett.*, vol. 16, pp. 2195–2198, 2017.



Derek Caudill received the B.S. degree in electrical engineering and the M.S. degree in electrical and computer engineering from the University of Massachusetts at Amherst, Amherst, MA, USA, in 2016 and 2017, respectively.

As a Researcher at the Communications Technology Laboratory, National Institute of Standards and Technology (NIST), Boulder, CO, USA, he supports the data acquisition efforts of millimeter-wave (mmWave) channel model measurements and the systems that such measurements depend on.



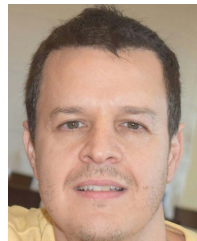
Jack Chuang received the Ph.D. degree from Pennsylvania State University, State College, PA, USA, in 2008.

He was a Graduate Research Assistant with the Communications and Space Sciences Laboratory (CSSL), Pennsylvania State University. He then worked at BAE Systems, Merrimack, NH, USA, in electronic warfare and Cisco Systems, Richfield, OH, USA, in spectrum sharing. He is currently with the Communication Technology Laboratory, National Institute of Standards and Technology (NIST), Gaithersburg, MA, USA, developing 5G millimeter-wave (mmWave) channel sounders.



Sung Yun Jun (Member, IEEE) received the Ph.D. degree in electronic engineering from the University of Kent, Canterbury, U.K., in 2018.

Since 2018, he has been a Post-Doctoral Associate with the RF Technology Division, National Institute of Standards and Technology, Boulder, CO, USA. His current research interests include antennas, microwave devices, and channel measurements and modeling of radio propagation.



Camillo Gentile (Member, IEEE) received the Ph.D. degree in electrical engineering from Pennsylvania State University, State College, PA, USA, in 2001, with a dissertation on computer vision and artificial intelligence.

He joined the National Institute of Standards and Technology, Gaithersburg, MA, USA, in 2001, where he is currently leading the Communications Technology Laboratory, Radio Access and Propagation Metrology Group. He has authored over 90 peer-reviewed journal articles and conference papers, a book on geolocation techniques, and a book on millimeter-wave channel modeling. His current interests include channel modeling and physical-layer modeling for 5G and 6G communications systems.



Nada Golmie (Senior Member, IEEE) received the Ph.D. degree in computer science from the University of Maryland at College Park, College Park, MD, USA, in 2002.

Since 1993, she has been a Research Engineer at the National Institute of Standards and Technology, Gaithersburg, MA, USA. She is currently an NIST Fellow and is currently the Chief of the Communications Technology Laboratory, Wireless Networks Division. Her research in media access control and protocols for wireless networks led to over 100 technical articles presented at professional conferences, journals, and contributed to international standard organizations and industry-led consortia. She is the author of the book *Coexistence in Wireless Networks: Challenges and System-level Solutions in the Unlicensed Bands* (Cambridge University Press, 2006). She leads several projects related to the modeling and evaluation of future generation wireless systems and protocols.

Dr. Golmie serves as the Co-Chair for the Next5G Channel Model Alliance.